A&A 466, 1089–1098 (2007)
DOI: 10.1051/0004-6361:20065588

Astronomy & Astrophysics

The Ca II infrared triplet as a stellar activity diagnostic

II. Test and calibration with high resolution observations⋆,⋆⋆

I. Busà[1], R. Aznar Cuadrado[2], L. Terranegra[3], V. Andretta[3], and M. T. Gomez[3]

[1] Istituto Nazionale di Astrofisica – Osservatorio Astrofisico di Catania, via S. Sofia 78, 95123 Catania, Italy
e-mail: ebu@oact.inaf.it
[2] Max-Planck-Institut für Sonnensystemforschung, Max-Planck-Str. 2, 37191 Katlenburg-Lindau, Germany
e-mail: aznar@mps.mpg.de
[3] Istituto Nazionale di Astrofisica – Osservatorio Astronomico di Capodimonte, Salita Moiariello 16, 80131 Napoli, Italy
e-mail: [andretta;gomez;terranegra]@na.astro.it

Received 11 May 2006 / Accepted 24 January 2007

ABSTRACT

Aims. We report on our analysis of the high resolution spectra ($R \approx 86\,000$) of a sample of 42 late-type active stars (with measured $\log R'_{\rm HK}$ spanning from ≈ -3 to ≈ -5) acquired with the Italian 3.6 m Telescopio Nazionale Galileo (TNG) using the SARG spectrometer in the 4960–10 110 Å range. The high quality of the spectra and the good activity-level coverage allow us to measure two different chromospheric indicators that can be derived from the Ca II infrared triplet (Ca II IRT) lines: the residual equivalent width (EQW) and the chromospheric indicator $R_{\rm IRT}$. The aim of this work is determine and test the best way of deriving activity-level information and errors from the Ca II IRT lines, in preparation of the GAIA Cornerstone mission by ESA, by which the Ca II IRT spectral range will be spectroscopically observed for millions of stars.
Methods. The $R_{\rm IRT}$ index is calculated for each observed star as the difference between the calculated NLTE photospheric central intensity and the observed one. The residual EQW, $\Delta W_{\rm IRT}$, is calculated as the area of the positive profile obtained as the difference between the calculated NLTE photospheric and the observed profiles. We correlate $\log R'_{\rm HK}$ with $R_{\rm IRT}$ and the $\Delta W_{\rm IRT}$.
Results. This analysis indicates that Ca II IRT lines are good chromospheric diagnostics. We find that both $\Delta W_{\rm IRT}$ and the $R_{\rm IRT}$ quantities can be used as chromospheric indicators, although the former exhibits a tighter correlation with the $\log R'_{\rm HK}$ index. Furthermore, we find that the total chromospheric excess EQW in the Ca II IRT is almost linearly correlated with the excess in the Ca II H & K doublet, as estimated through the $\log R'_{\rm HK}$ index.

Key words. stars: atmospheres – radiative transfer – line: formation – stars: chromospheres – stars: activity

1. Introduction

Magnetically-induced stellar activity is thought to have its roots in the interaction of stellar rotation and turbulence. This interaction is believed to lead to the amplification of the magnetic field by dynamo processes in the interior of the stars, which, in the uppermost layers of stellar atmospheres, manifests itself in the many stellar-activity phenomena such as star spots, chromospheric plages, ultraviolet, and X-ray emission (Hempelmann et al. 1996). The amounts of radiation originating from different temperature intervals in these outer atmospheres (i.e., the chromosphere, the corona, and the transition region) have been used to measure magnetic activity; well-known examples are the chromospheric Ca II H & K line core emission and the coronal X-ray emission (Piters et al. 1997). Furthermore, the emission fluxes of the activity diagnostics formed in the different layers of a stellar atmosphere correlate with rotational period, age, and with each other; empirical relations have been obtained for well-known activity indicators, $L_{\rm X} \propto L_{\rm CIV}^{1.4} \propto L_{\rm MgII}^{2.24} \propto \Delta V_{\rm max}$ (see, e.g., Rodonò 2000, and references therein).

The discovery of the Ca II H & K emission reversal as a chromospheric activity indicator occurred at the beginning of the last century when Hale & Ellerman (1920) showed it to be related to solar plage regions and connected to active stellar chromospheres as argued by Eberhard & Schwarzschild (1913). After these pioneering works, many observations of the H and K lines have provided a wealth of information on stellar chromospheres demonstrating the now firmly established connections of the Ca II emission flux to the magnetic dynamo.

The lines of the Ca II infrared triplet (Ca II IRT) $\lambda\lambda$ 8498, 8542, 8662, which share the upper level of the H and K transitions, are similar to the H & K lines in many respects. In particular, theoretical investigation based on semi-empirical chromospheric modelling of the quiescent solar atmosphere, show that the Ca II IRT accounts for at least the same amount of net cooling losses as the H & K lines (see, e.g., Vernazza et al. 1981, Table 29). On the other hand, empirical studies of active stars on a wide range of activity levels suggest that, in fact, the contribution of the Ca II IRT to the total chromospheric radiative losses can be even twice as the contribution of the H & K lines (see, e.g., Dempsey et al. 1993). If we consider that, all together, the calcium lines significantly contribute to the total chromospheric losses in solar-type stars and that the contribution is usually not

⋆ Based on observations made with the Italian Telescopio Nazionale Galileo (TNG) operated on the island of La Palma by the Centro Galileo Galilei of the Consorzio Nazionale per l'Astronomia e l'Astrofisica at the Spanish Observatorio del Roque de los Muchachos of the Instituto de Astrofísica de Canarias.
⋆⋆ Table 4 is only available in electronic form at http://www.aanda.org

much smaller than the normally dominating Mg II h & k lines (see, e.g., Linsky 1991, Table 1), we expect that the Ca II IRT could provide useful information on the energy balance of stellar chromospheres.

Furthermore, from an observer's point of view, the Ca II IRT presents some advantages over the Ca II H & K. Unlike the blue Ca II lines, for instance, the IRT lies in a region of the spectrum with a well-defined continuum, making normalization simpler, and they are not significally affected by telluric lines. In recent years, moreover, with advances in the technology of detectors sensitive to the (near-)IR, the Ca II IRT lines are becoming more and more extensively observed.

It is not surprising, therefore, that the diagnostic power of the Ca II IRT lines as magnetic activity indicators has been investigated by many authors. Linsky et al. (1979) showed, for example, that the radiative loss rates in the λ8542 line correlate well with radiative loss rates in the Ca II H & K and Mg II h & k lines, while Chmielewski (2000) find an average relation between the central depth of the observed λ8542 line and the $\log R'_{\rm HK}$ indicator. However, as Chmielewski stresses, the observed central depressions (*CD*) cannot be considered pure chromospheric indicators because no correction for the photospheric contribution has been made. The proper subtraction of the photospheric quiescent contribution is in fact essential for correctly defining any chromospheric activity indicator. In the first paper of this series, Andretta et al. (2005) suggested that the $R_{\rm IRT}$ index is a better estimator of the chromospheric contribution to the Ca II IRT lines that takes into account the proper subtraction of the photospheric quiescent contribution.

The Ca II IRT is useful not only for studies of stellar chromospheric activity (for a short summary see, e.g., Andretta et al. 2005). The versatility of those spectral features has contributed to the selection of the 8480–8740 Å wavelength range for the medium resolution spectrograph of the GAIA mission (the GAIA Radial Velocity Spectrometer, RVS). The GAIA mission, which was reconfirmed within the ESA Cosmic Vision 2020 science program for a launch date in mid-2011 and final catalogues foreseen in 2018, will collect the spectra of about 150 million stars up to magnitude $V = 17$ (Katz et al. 2004).

In the context of the study of chromospheric activity, therefore, the GAIA galactic survey of the Ca II IRT could provide direct and quick information on stellar activity levels, together with important information about the stars' mass, age, convection, and rotation. From this perspective, a preparatory study aimed to define, calibrate, and test possible candidate activity indicators using these lines would be very useful.

Measurement of activity level can also help in avoiding errors in applying the GAIA standard classification method to active stars. This is particularly true for metal-poor stars, for which determination of the atmospheric parameters will be based mainly on the Ca II IRT lines. Furthermore, stellar activity must be taken into account to avoid false alarms for some tasks concerning science alerts, peculiar objects, and planetary transit determination. This observing program has been developed with this in mind.

In this paper, we report on our analysis of the high resolution spectra of a sample of 42 late-type active stars to test, calibrate, and compare two different candidates for chromospheric activity indicators that can be derived from the Ca II IRT lines: the $R_{\rm IRT}$ and the residual equivalent width (EQW), which we denote in this paper by $\Delta W_{\rm IRT}$.

2. Observations and data reduction

We observed 42 stars spanning a wide range of activity levels. The stars (except for HD 26736, HD 28805, and HD 29461) were selected from the Strassmeier et al. (2000) catalog, which gives the $\log R'_{\rm HK}$ measurements, $T_{\rm eff}$, projected rotational velocity ($v \sin \hat{\imath}$), and radial velocity for each star.

The observations were collected with the SARG (Gratton et al. 2001), the high-dispersion spectrograph at the 3.6 m TNG in La Palma (Spain), on February 22 and 23, 2002. The 42 late-type stars included spectral types from F5 to K3.

SARG is a single-arm, white-pupil, cross-dispersed echelle spectrograph, mounted on one of the arms of the TNG fork. The present observations were made using the RED cross-dispersed grism mounted on SARG, which provides a spectral coverage from 5500 to 10 110 Å, with a gap of about 40 Å, due to the non-sensitive region between the two $4K \times 2K$ thinned, back-illuminated EEV CCDs located in the focal plane of the spectrograph. The CCDs, with a pixel size of 13.5 μm, were binned to 2×1. The minimum interorder separation is about 6 arcsec. These observations were obtained using a slit width of 100 μm, corresponding to 0.53 arcsec projected on the sky, yielding a spectral resolution ($\lambda/\Delta\lambda$) of 86 000.

All of the stellar spectra were bias-subtracted, flat-fielded, and then cleaned of cosmic ray events. Images were corrected for scattered light, and 51 orders were defined, traced, and extracted. One-dimensional spectra were extracted using standard IRAF[1] routines for echelle spectra. Several thorium lamp exposures were obtained during each night and then used to provide a wavelength calibration of the observations. Each spectral order was normalized by a polynomial fit to the local continuum. The 42 selected stars are listed in Table 1, together with some characteristics of the observations.

In Fig. 1 we show the reduced spectra in the Ca II IRT range for the most active stars of our sample. The spectra are ordered according to increasing values of $\log R'_{\rm HK}$. It is worthwhile to notice (see Fig. 1) that, with increasing activity level, the lines show intense filled-in absorption, which becomes strong reversal emission in the cores of very active K stars such as HD 82443 and HD 175742. This is because the weaker continuum of K stars, compared to hotter stars, makes it easier for the IRT lines to show emission rather than filled-in absorption profiles.

Three stars of our sample – HD 68638, HD 79969, and HD 132756 – show double-lined spectroscopic binary signatures in our high-resolution spectra. The first was reported as a single-line spectroscopic binary by Latham et al. (2002), the second was identified as a double star by Horch et al. (2002), and the last was reported as a double-lined spectroscopic binary by Goldberg et al. (2002). HD 65430 is referred to as a spectroscopic binary in Nidever et al. (2002). Stars HD 47157, HD 98736, HD 108574, and HD 149806 are flagged as double systems in the SIMBAD database. Santos et al. (2003) reported HD 128311 as a planet host star.

We will only consider the first four stars as spectroscopic binaries (i.e., HD 65430, HD 68638, HD 79969, and HD 132756). Stars HD 25998, HD 43989, HD 129674, HD 171488, and HD 175742 appear to be fast rotators with very broad lines in our high-resolution spectra.

[1] IRAF is distributed by the National Optical Astronomy Observatories, which are operated by the Association of Universities for Research in Astronomy, Inc., under contract with the National Science Foundation.

Table 1. Details of SARG observations.

Target	HJD (+2 452 300)	t_{exp} (s)	V	T_{sp}	$\log R'_{HK}$
HD 14798	28.351	900	8.0	K0V	–5.30
HD 25998	28.366	300	5.5	F7V	–4.27
HD 26736	29.356	1200	8.1	G5V	—
HD 28495	29.468	1200	7.8	G0V	–4.03
HD 28805	29.379	1500	8.7	G5V	—
HD 29461	29.397	1200	7.9	G5V	—
HD 31000	28.381	1200	7.8	G5V	–4.09
HD 43989	29.339	1200	8.0	G0V	–3.82
HD 47157	28.410	1800	7.6	G5V	–4.82
HD 58781	29.506	1000	7.3	G5V	–4.80
HD 59747	29.425	1200	7.7	G5V	–4.19
HD 64468	29.448	1500	7.8	K2V	–5.00
HD 65430	29.491	1200	7.7	K0V	–4.85
HD 68638	28.585	1500	7.5	G8V	–4.68
HD 72760	29.522	900	7.3	G5V	–4.21
HD 72946	29.538	1000	7.3	G5V	–4.89
HD 76752	28.543	1200	7.5	G2V	–4.74
HD 76780	28.565	1500	7.6	G5V	–4.58
HD 79969	29.553	900	7.2	K3V	–4.44
HD 81040	29.569	1200	7.7	G0V	–4.47
HD 82443	28.497	1200	7.0	K0V	–4.02
HIP 46854	29.598	2400	9.4	K0V	–5.52
HD 91148	28.520	1800	7.9	G8V	–4.48
HD 94765	29.624	1200	7.7	K0V	–4.34
HD 96937	29.642	1200	7.7	G5V	–4.58
HD 98736	28.727	1200	8.0	G5V	–4.96
HD 105631	29.729	1200	7.5	K0V	–4.50
HD 108574	28.703	1200	7.4	F5V	–4.25
HD 110833	28.681	1200	7.0	K3V	–4.52
HD 112742	28.629	1500	7.6	K0V	–5.10
HD 116442	29.658	900	7.1	G5V	–4.72
HD 119332	29.748	1200	7.8	K0IV-V	–4.55
HD 122676	29.677	900	7.1	G5V	–4.70
HD 128311	29.709	1200	7.5	K0V-K3V	–4.30
HD 129674	29.763	1000	7.5	F0V	–4.30
HD 131023	28.744	900	7.4	K0V	–4.39
HD 132756	29.690	1000	7.3	G0V	–4.70
HD 149806	29.804	900	7.1	K0V	–4.62
HD 164922	28.785	900	7.0	K0V	–4.92
HD 165807	28.801	1000	7.5	K0V	–5.44
HD 171488	28.769	1000	7.4	G0V-G2V	–3.74
HD 175742	29.782	1500	8.1	K0V	–3.89

Table 2 presents the physical parameters of our sample of stars collected from the literature. The first column shows the ID (HD numbers for all stars, except for HIP 46854 for which no HD number is defined) of the targets. The second and third columns give iron abundances determined from spectral analysis and metallicities determined from photometry, and the fourth column provides surface gravity derived from photometry. The fifth column gives effective temperatures derived from photometry, while the sixth column reports the projected rotational velocity.

3. Activity indicators from the Ca II IRT

The infrared triplet lines of ionized calcium (Ca II IRT) at 8498, 8542, and 8662 Å are prominent figures in the spectra of late-type stars. Their extended wings probe a wide range of photospheric layers and are sensitive to the temperature distribution in the atmosphere of the star (Andretta et al. 2005). Their cores are formed in the uppermost atmospheric layers (chromosphere), hence, their central depressions (CD) are sensitive to the degree of activity in their outer layers (see, e.g., the relation between CD and the Mount-Wilson chromospheric activity indicator R'_{HK} by Chmielewski 2000).

However, there are some problems in the use of the Ca II IRT lines as chromospheric diagnostics. These are the dependence of CD on $v \sin \hat{\imath}$ and the photospheric contribution. Contrary to the very broad Ca II H & K lines, the narrow cores of the Ca II IRT are broadened by rotation, even for relatively slow rotators. This effect has always been either neglected (as in, e.g., Linsky et al. 1979; Dempsey et al. 1993) or even ignored (as in, e.g., Foing et al. 1989; Chmielewski 2000). For example, a value of $v \sin \hat{\imath} = 10\,\mathrm{km\,s^{-1}}$ raises the photospheric CD of the Ca II IRT line at λ8542, in a star characterized by $T_{eff} = 5200$ K, $\log g = 4.0$, and solar metalicity, of about 0.11, a value comparable to the estimated chromospheric filling-in of a somewhat active star. Furthermore, the proper subtraction of the photospheric contribution is essential for correctly estimating of the chromospheric contribution to any activity diagnostic.

The $\log R'_{HK}$ diagnostic in Strassmeier et al. (2000), which will be used to calibrate our indicators, is derived with the method of Linsky et al. (1979). It includes the correction for the photospheric contribution by subtracting, from the absolute Ca II H & K fluxes, the flux obtained using partial redistribution radiative transfer (cf. Kelch et al. 1979) in a radiative equilibrium atmosphere. Log R'_{HK}, therefore, represents a purely chromospheric emission indicator.

To derive pure chromospheric diagnostics from the Ca II IRT lines, computed line profiles from the radiative equilibrium atmosphere are required. The NLTE line synthesis in photospheric models permits us to address both problems. By comparing the NLTE-$v \sin \hat{\imath}$-convolved synthetic line with the observed profile, we obtain information on the purely chromospheric contribution. In particular, this is done by measuring two possible candidates for chromospheric indicators: (i) the R_{IRT} index given by the difference between the observed CD and computed, $v \sin \hat{\imath}$-convolved CD_{conv}(NLTE); and (ii) the core-residual EQW given by the area of the positive profile obtained as the difference between the calculated NLTE-$v \sin \hat{\imath}$-convolved photospheric and the observed profiles.

3.1. NLTE photospheric line profiles

In order to calculate the R_{IRT} index and the core-residual EQW, we need to calculate the theoretical photospheric Ca II IRT profiles. Therefore, for each star, we considered the NLTE formation of the Ca II IRT lines in a photospheric model of a stellar atmosphere selected from the Next-Gen database (Allard & Hauschildt 1995) according the physical parameters (T_{eff}, $\log g$, [A/H], and $v \sin \hat{\imath}$). We used the Next-Gen model grid[2] available online, which has a 200 K step for T_{eff}, 0.5 step for $\log g$, and 1.0 step for [A/H]. We verified that a tight grid is not necessary due to the weak dependence of both core EQW and CD depression on stellar parameters (see Andretta et al. 2005).

Not all the needed parameters are available in the literature for most of the stars (see Table 2). Therefore, to select the most appropriate photospheric model for each star, we considered a grid of four-to-eight Next-Gen atmospheric models spanning the range around the expected values according the Table B1 in Gray (1992) and the spectral type of the star. We therefore selected the atmospheric model in which radiative transfer calculations give Ca II IRT profiles that best-fit the wings of the

[2] http://www.hs.uni-hamburg.de/EN/For/ThA/phoenix/index.html

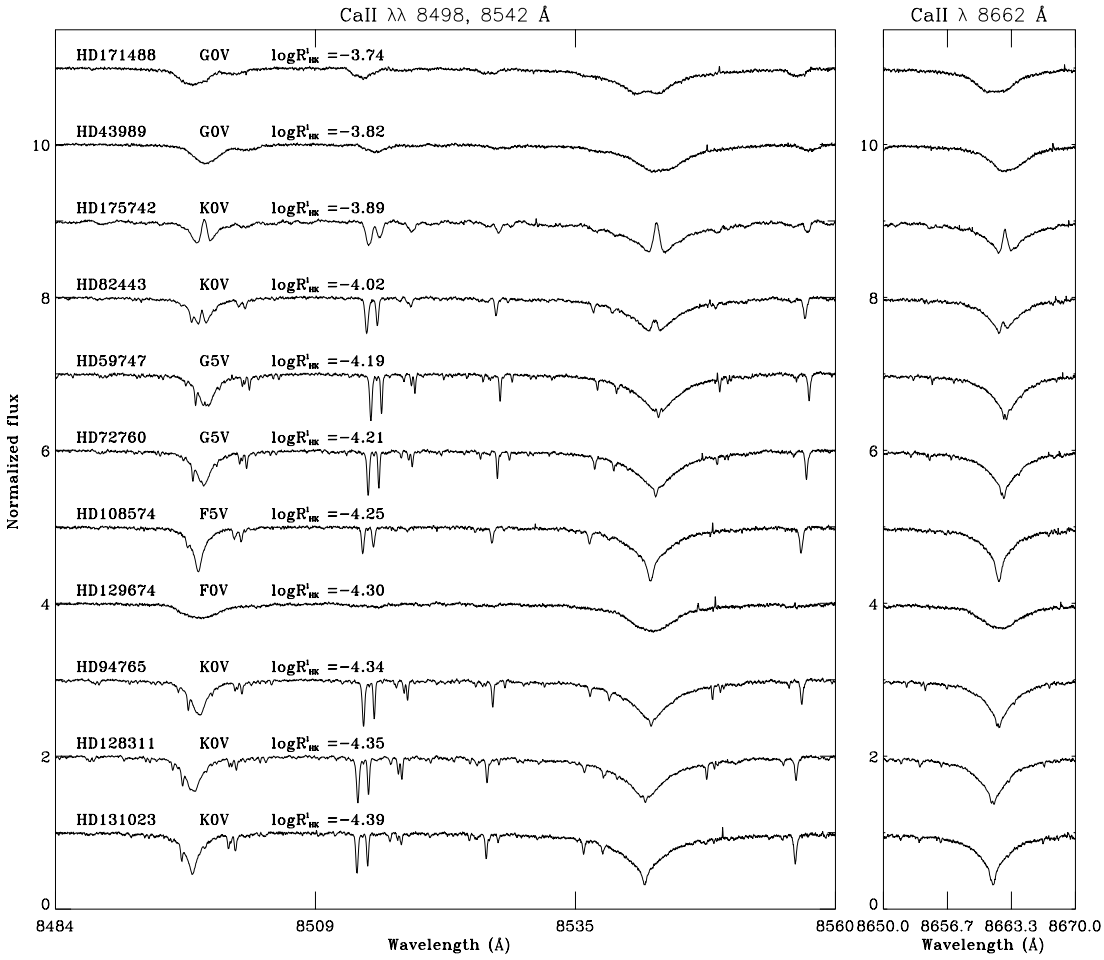

Fig. 1. SARG spectra, in the region of the Ca II infrared triplet, of the thirteen most active observed stars. The spectra are ordered (*from bottom to top*) according to increasing values of $\log R'_{\rm HK}$.

observed Ca II IRT profiles. The choice of the atmospheric model that describes each star best was mainly based on fitting the Ca II IRT λ8662 line whose profile shows a higher sensitivity to stellar parameters than do the other two Ca II IRT lines.

For all of the stars, the metallicity derived from the fitting procedure is zero. This is due to the grid of models used here where only [A/H] = 0, −1, −2 are considered. Nevertheless, because the metallicity contributes to the wing formation of the Ca II IRT lines, while its contribution to the core is negligible (Andretta et al. 2005), a higher precision in the models of [A/H] is not necessary in this work. Table 3 shows the values of $T_{\rm eff}$, $\log g$, and $v \sin \hat{\imath}$ selected by the fitting procedure for each star.

For one star in our sample, HD 129674, there is no $v \sin \hat{\imath}$ measurement in the literature. In this case, even if we know that the obtained value is only an approximate estimate, $v \sin \hat{\imath}$ = 85 km s^{-1} (as reported in Table 3) has been inferred from the fit of the Ca II IRT lines.

Figure 2 shows as an example the λ8662 line fitting for the G5 V star HD 31000 for which both metallicity and $\log g$ are unknown. Table B1 in Gray (1992) predicts $T_{\rm eff}$ = 5678 K and $\log g$ = 4.46 for a G5 main-sequence star. Taking the measured value of $T_{\rm eff}$ = 5420 K into account, we considered four possible models combining the fixed values of $T_{\rm eff}$ = 5400 K and $v \sin \hat{\imath}$ = 7.5 with $\log g$ = 4.5 or 4.0, and [A/H] = 0.0 or −1.0. The four synthetic lines (obtained from an NLTE radiative transfer model, with rotational and instrumental convolution) are plotted against the observed profile in the top panel of the figure. In the bottom panel we plot the residuals for the two best-fitting synthetic lines; the comparison of the residuals in the wings closer to the line core lets us select the atmospheric model with $T_{\rm eff}$ = 5400, $\log g$ = 4.5, and [A/H] = 0.0.

For the selected atmospheric models of Table 3, the coupled equations of radiative transfer and statistical equilibrium were solved using version 2.2 of the code MULTI (Carlsson 1986) for a Ca atomic model that incorporates eight levels of Ca I, the lowest five levels of Ca II, and the ground state of Ca III. Nine b-b and thirteen b-f transitions are treated in detail. Collisional data are the same as those used by Drake (1991).

The calculations were done using complete redistribution approximation for the line source-functions of the Ca II IRT lines, which is a good assumption for these lines due to their deep formation compared to the Ca II H & K lines, for which partial redistribution is important (Uitenbroek 1989). The continuum opacity package included in the code takes free-free opacity into account, Rayleigh scattering, and bound-free transitions for hydrogen and metals. We do not take into account the treatment of line-blanketing (see, e.g., Busà et al. 2001), because we find that, in the range of stellar parameters of interest, the UV missing opacity does not appreciably affect the Ca II IRT line formation. The adopted calcium abundance is $\log \epsilon_{\odot}$(Ca) = 6.34 (Chmielewski 2000).

We did not solve the hydrostatic equilibrium equation (HSE) in the hydrogen computation to recompute the electron density from the original temperature distribution as is usually done in

Table 2. Physical parameters collected from the literature.

ID	[Fe/H]	[M/H]	log g_{phot}	T_{eff} (K)	$v \sin i$ (km s^{-1})
HD 14798				4700[1]	3[1]
HD 25998		−0.11 ± 0.10[2], 0.12 ± 0.10[5]	4.35 ± 0.10[2], 4.37 ± 0.10[5]	6147 ± 50[2], 6360 ± 80[5], 6184 ± 53[3], 6200[1]	16[1]
HD 26736	0.09[25]		4.4[25], 4.42[26]	5729[26], 5750[25]	5.4[25]
HD 28495				5390[1]	5.4[1]
HD 28805	0.08[25]	0.21 ± 0.10[10]	4.45[26], 4.5[25]	5451[26], 5500[25]	3.8[25]
HD 29461	0.12[23]		4.42[26]	5690[26], 5150[27]	
HD 31000				5420[1]	7.5[1]
HD 43989				5930[1], 5900[7]	40 ± 0.4[6], 47[14], 25–42[7⋆]
HD 47157				5450[1]	10.7[1]
HD 58781				5480[1]	5.2[1]
HD 59747	−0.14[23]			5140[1]	5.1[24]
HD 64468				4950[1]	2.8[1]
HD 65430	−0.09[18]	0.25 ± 0.10[11]		5210[1]	4.7[1]
HD 68638	−0.27[18]			5420[1]	7.5[1]
HD 72760		0.04 ± 0.10[11]		5310[1], 5210[15]	4.2[15], 8[1]
HD 72946	0.09 ± 0.07[3], 0.24 ± 0.10[4], 0.07[18]	0.40 ± 0.10[4]	4.4 ± 0.2[4†]	5695 ± 58[3], 5530[1], 5911 ± 50[4]	3.5 ± 0.8[13], 9.4[1]
HD 76752				5630[1]	4.8[1]
HD 76780	0.09 ± 0.08[3], 0.21 ± 0.10[4]	0.30 ± 0.10[4]	4.3 ± 0.2[4†]	5700 ± 77[3], 5590[1], 5869 ± 50[4]	7.6[1]
HD 79969				4870[1]	5.1 ± 0.8[13], 5.7[1]
HD 81040				5630[1]	3.7[1]
HD 82443		–0.14 ± 0.10[11]		5340[1], 5240[15]	7.3[1], 6.2[9,23], 6.5[14]
HIP46854				4510[1]	7[1]
HD 91148				5530[1]	6.8[1]
HD 94765		0.09 ± 0.10[11]		5010[1]	1[16], 6.5[1]
HD 96937				5340[1]	5.5[1]
HD 98736				5070[1]	6.4[1]
HD 105631		0.16 ± 0.10[11]		5310[1]	3[1]
HD 108574				5970[1]	7.6[1]
HD 110833	–0.17[18]			4970[1], 5000[17]	3[1]
HD 112742				4850[1]	4.9[1]
HD 116442				5340[1]	4.4[1]
HD 119332				5210[1]	5.8[1]
HD 122676				5450[1]	5[1]
HD 128311	0.10 ± 0.10[22♡]	0.08 ± 0.10[11]	4.8 ± 0.15[22♡]	4910[1], 4950 ± 50[22♡]	4.9[1]
HD 129674				6730[1]	
HD 131023				5390[1]	4.8[1]
HD 132756	–0.5[19], –0.32[20], –0.57[21♣]		4.74[21♣]	5590[1], 5500[19‡], 5345[21♣]	2[1], 4[19‡]
HD 149806				5210[1]	6.2[1]
HD 164922				5290[1]	4.6[1]
HD 165807				4520[1]	7.5[1]
HD 171488				5820[1]	33[8], 36[1], 45[12], 40[14], 38[7,10], 39 ± 0.4[6]
HD 175742		–0.70 ± 0.10[11]		5030[1]	14.6[1]

References: [1] Strassmeier et al. (2000), [2] Chen et al. (2000), [3] Taylor (2003), [4] Feltzing & Gustafsson (1998), [5] Gray et al. (2001), [6] Wichmann et al. (2003), [7] Osten & Saar (1998), [8] Henry et al. (1995), [9] Fekel (1997), [10] Kotoneva et al. (2002), [11] Haywood (2001), [12] Cutispoto et al. (2002), [13] Tokovinin & Smekhov (2002), [14] Messina et al. (2001), [15] Gaidos et al. (2000), [16] Song et al. (2002), [17] Habing et al. (2001), [18] Eggen (1998), [19] Goldberg et al. (2002), [20] Beers et al. (1999), [21] Snider et al. (2001), [22] Santos et al. (2003), [23] Nordström et al. (2004),[24] Głębocki & Stawikowski (2000), [25] Paulson et al. (2003), [26] Thorburn et al. (1993), and [27] Wright et al. (2003).

⋆ Reference 7 gives two possible solutions for HD 43989: double subgiant (G0 IV + G0 IV, T_{eff} = 5900 K, $v \sin \hat{i}$ = 25 km s^{-1} each) and a single subgiant with the same T_{eff} and $v \sin \hat{i}$ = 42 km s^{-1}.

† Reference 4 gives values of surface gravity as derived from spectroscopy for HD 72946 (log g_{spec} = 5.0±0.2) and HD 76780 (log g_{spec} = 4.8±0.2).

‡ Reference 19 reports HD 132756 as a double-lined spectroscopic binary with effective temperatures T_{eff}^{1} = 5500 K and T_{eff}^{2} = 5250 K, both components with $v \sin i$ = 4 km s^{-1}.

♣,♡ Atmospheric parameters derived from spectroscopic data.

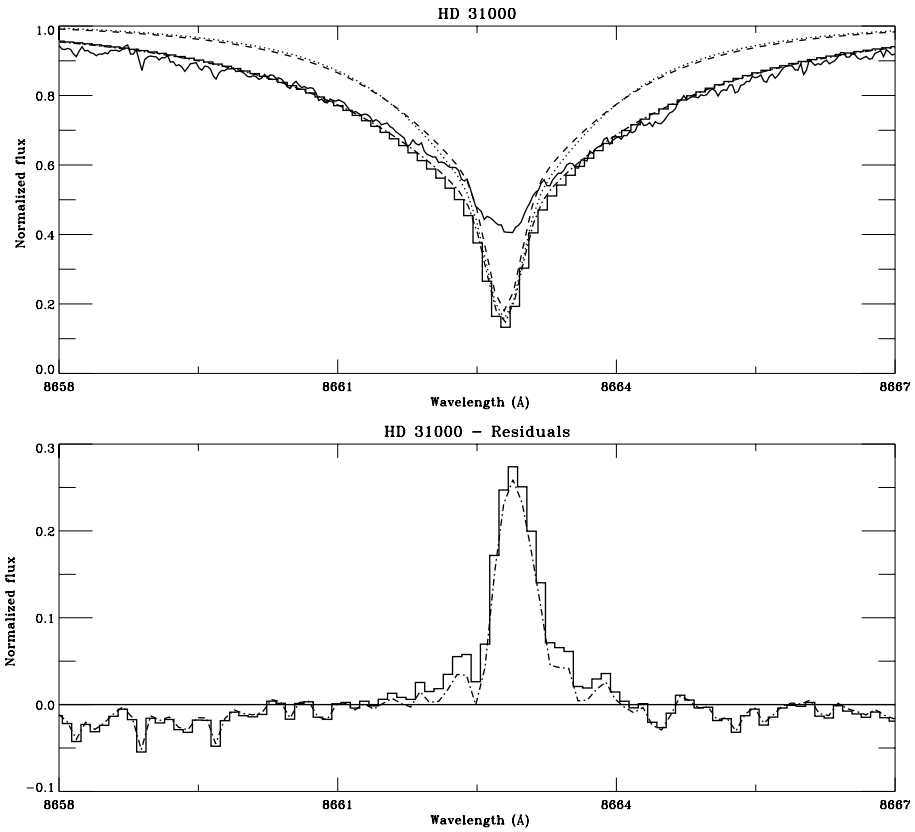

Fig. 2. *Top panel*: NLTE computed Ca II IRT λ8662 profiles compared with observations (solid line) of HD 31000. The dotted line represents the profile obtained from the model with $T_{\rm eff}$ = 5400 K, $\log g$ = 4.0, and [A/H] = −1; the dashed line refers to the $T_{\rm eff}$ = 5400 K, $\log g$ = 4.5, and [A/H] = −1 model; dot-dashed line to the $T_{\rm eff}$ = 5400 K, $\log g$ = 4.5, and [A/H] = 0 model; and histogram to the $T_{\rm eff}$ = 5400 K, $\log g$ = 4.0, and [A/H] = 0 model. *Bottom panel*: residuals (observed flux minus synthetic flux) of the two best-fitting synthetic lines obtained from the $T_{\rm eff}$ = 5400 K, $\log g$ = 4.5, and [A/H] = 0 (dash-dotted line), and $T_{\rm eff}$ = 5400 K, $\log g$ = 4.0, and [A/H] = 0 (histogram) models.

the treatment of NLTE upper atmosphere line synthesis. This is because the photospheric electron densities of the Next-Gen models are calculated in HSE consistently with the total opacity including LTE line-blanketing. If we would have imposed HSE in our NLTE computation, the lack of opacity due to the crowding of lines would give higher $\mathrm{d}P/\mathrm{d}\tau$ with respect to the LTE model ($\mathrm{d}P/\mathrm{d}\tau \propto 1/\kappa$, where κ is the total opacity), and therefore a higher and not correct gradient $\mathrm{d}N_{\rm e}/\mathrm{d}\tau$ since $P \propto N_{\rm e}$.

Each of the Ca II IRT line profiles thus obtained, was convolved with the proper instrumental profile and, for each target star, with the stellar rotational broadening profile. These NLTE, $v \sin \hat{\imath}$-convolved radiative-equilibrium profiles were then used to measure the CD, $R_{\rm IRT}$, and $\Delta W_{\rm IRT}$, as described in the following section.

3.2. Central depression and equivalent width measurements and associated errors

The measurements of the three quantities of interest, the central depression (CD), the $R_{\rm IRT}$ index, and the residual EQW, $\Delta W_{\rm IRT}$, are all based on the observed profiles, $F(\lambda)$, normalized to the local continuum, $F_{\rm c}$:

$$r(\lambda) \equiv \frac{F(\lambda)}{F_{\rm c}}. \tag{1}$$

Thus, the CD is:

$$CD \equiv 1 - \langle r(\lambda_\circ)\rangle, \tag{2}$$

where $\lambda_\circ$ is the central core wavelength, determined empirically from a polynomial fit around the line center, a procedure needed because many stars show noticeable profile asymmetries. The line depth $\langle r(\lambda_\circ)\rangle$ is estimated by a three-point average around $\lambda_\circ$ ($\lambda_\circ$ plus one point on each side of $\lambda_\circ$).

The $R_{\rm IRT}$ index is then determined as follows (see Andretta et al. 2005):

$$R_{\rm IRT} \equiv CD_{\rm th} - CD = \langle r(\lambda_\circ)\rangle - r_{\rm th}(\lambda_\circ), \tag{3}$$

where $CD_{\rm th}$ is the central depression at $\lambda_\circ$ of the theoretical NLTE photospheric profile, $r_{\rm th}(\lambda)$, broadened to account for both instrumental resolution and stellar rotation.

Finally, the residual EQW is obtained by integrating the difference of the observed and theoretical photospheric profiles

$$\Delta W_{\rm IRT} \equiv \int_{\Delta\lambda} [r(\lambda) - r_{\rm th}(\lambda)]\,\mathrm{d}\lambda, \tag{4}$$

over a wavelength band, $\Delta\lambda$ covering the line core. For our sample of stars, $\Delta\lambda$ goes from 0.1 Å in slow-rotating, non-active stars, up to 6 Å, in fast rotators and/or very active stars. An example of $\Delta W_{\rm IRT}$ measurement is shown in Fig. 3.

The uncertainty associated to the three quantities CD, $R_{\rm IRT}$, and $\Delta W_{\rm IRT}$ can be derived from the respective definitions assuming that the main source of error is the statistical noise in the observed normalized profile. From Eq. (1),

$$\sigma^2[r(\lambda)] = r^2(\lambda)\left(\frac{\sigma^2[F(\lambda)]}{F^2(\lambda)} + \frac{\sigma^2[F_{\rm c}]}{F_{\rm c}^2}\right).$$

From the knowledge of the *S/N* ratio of the spectrum ($S/N \equiv F_{\rm c}/\sigma[F_{\rm c}]$), the above equation becomes

$$\sigma^2[r(\lambda)] = \frac{r^2(\lambda)}{(S/N)^2}\left(1 + \frac{F_{\rm c}^2}{F^2(\lambda)}\frac{\sigma^2[F(\lambda)]}{\sigma^2[F_{\rm c}]}\right).$$

Finally, assuming a Poisson error statistics for flux errors, i.e., $\sigma^2[F(\lambda)] \propto F(\lambda)$, which means $\sigma^2[F(\lambda)]/F(\lambda) = \sigma^2[F_{\rm c}]/F_{\rm c}$, we obtain:

$$\sigma^2[r(\lambda)] = \frac{r(\lambda)\,(1 + r(\lambda))}{(S/N)^2}. \tag{5}$$

Table 3. Temperature, gravity, and projected rotational velocity for each star, selected for the NLTE line synthesis computation.

Target	$T_{\rm eff}$ (K)	$\log g$	$v \sin \hat{\imath}$ (km s^{-1})
HD 14798	4800	4.0	3.0
HD 25998	6400	4.5	16.0
HD 26736	5800	4.5	5.4
HD 28495	5400	4.5	5.4
HD 28805	5400	4.5	3.8
HD 29461	5600	4.5	3.0
HD 31000	5400	4.5	7.5
HD 43989	6000	4.5	40.0
HD 47157	5400	4.0	10.7
HD 58781	5400	4.5	5.2
HD 59747	5200	4.5	5.1
HD 64468	5000	4.5	2.8
HD 65430	5200	4.5	4.7
HD 68638	5400	4.5	7.5
HD 72760	5200	4.5	4.2
HD 72946	5800	4.5	3.5
HD 76752	5600	4.5	4.8
HD 76780	5800	4.5	7.6
HD 79969	4800	4.5	5.1
HD 81040	5600	4.5	3.7
HD 82443	5200	4.5	7.3
HIP 46854	4600	4.0	7.0
HD 91148	5600	4.5	6.8
HD 94765	5000	4.5	1.0
HD 96937	5400	4.5	5.5
HD 98736	5000	4.0	6.4
HD 105631	5400	4.5	3.0
HD 108574	6000	4.5	7.6
HD 110833	5000	4.5	3.0
HD 112742	4800	4.5	4.9
HD 116442	5400	4.5	4.4
HD 119332	5200	4.5	5.8
HD 122676	5400	4.5	5.0
HD 128311	5000	5.0	4.9
HD 129674	6800	4.0	85.0
HD 131023	5400	4.5	4.8
HD 132756	5600	4.5	2.0
HD 149806	5200	4.5	6.2
HD 164922	5200	4.5	4.6
HD 165807	4600	4.5	7.5
HD 171488	5800	4.5	33.0
HD 175742	5000	4.5	14.6

From Eq. (5), together with Eqs. (2) and (3), we obtain an expression for the uncertainty on the measurements of *CD* and $R_{\rm IRT}$:

$$\sigma[CD] = \sigma[R_{\rm IRT}] = \sigma[r(\lambda_\circ)]/\sqrt{3}. \quad (6)$$

In a numerical integration scheme with prescribed weights, w_i, the residual EQW defined in Eq. (4) is computed as follows:

$$\Delta W_{\rm IRT} \simeq \sum_i w_i \, [r(\lambda_i) - r_{\rm th}(\lambda_i)] \, \delta\lambda,$$

where $\delta\lambda$ is the wavelength spectral sampling, and the index i runs over the range of line core wavelengths. It follows that

$$\sigma^2[\Delta W_{\rm IRT}] = \delta\lambda^2 \, \sum_i w_i^2 \sigma^2[r(\lambda_i)]. \quad (7)$$

In a trapezoidal scheme, for instance, $w_i = 1$ for all i, except for the first and last points, where $w = 1/2$.

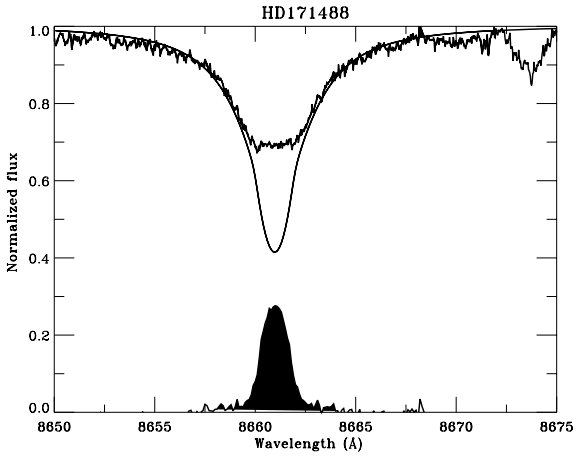

Fig. 3. EQW measurement method, with the example of HD 171488. The plot shows the synthetic photospheric line profile (thin solid line) superimposed on the observed profile (thick solid line). The filled-in profile is obtained as the smoothed difference between the two profiles. The residual EQW ($\Delta W_{\rm IRT}$) is measured as the area of the black filled-in profile.

The error estimates given in Eq. (6) neglect the uncertainty in the theoretical profile in the core, $r_{\rm th}(\lambda_\circ)$. However, Andretta et al. (2005) have shown that the core of the Ca II IRT lines exhibit only a weak dependence on stellar parameters, in the range of values valid for the present sample of stars. Thus, the only other, possibly significant, uncertainty comes from the broadening parameter, mainly $v \sin \hat{\imath}$. We, however, found that the statistical noise dominates this source of errors in our data. Thus, we adopted Eq. (6) for our error estimates without further ado.

In the case of the residual EQW, $\Delta W_{\rm IRT}$, errors in the theoretical line profiles may be larger, particularly in the "shoulders" of the line profile: both the uncertainties in the stellar parameters ($T_{\rm eff}$, $\log g$, [A/H]) and intrinsic uncertainties in the model photosphere may contribute to the uncertainties in the theoretical line profiles. Moreover, a possibly systematic source of error in the $\Delta W_{\rm IRT}$ in these cool stars could come from the presence of blends in the Ca II IRT lines due to the hydrogen Paschen lines: P16 λ8502.49 in the wing of Ca II IRTλ8498.02, P15 λ8545.39 in the wing of the Ca II IRTλ8542.09, and P13 λ8665.02 in the wing of the Ca II IRTλ8662.14 (Chmielewski 2000).

It is difficult to estimate the magnitude of the errors on $\Delta W_{\rm IRT}$ due to the uncertainties in the theoretical line profiles. A rough, yet still reasonable, estimate can be obtained considering, for each star, the measured $\Delta W_{\rm IRT}$ values that we obtain when adopting theoretical models that differ from the selected one (reported in Table 3) of 0.5 in $\log g$, 200 K in $T_{\rm eff}$, or 1.0 in [A/H]. We obtain $\Delta W_{\rm IRT}$ variations with respect to the Table 4 values up to 15% for $\log g$ variations, up to 4% for $T_{\rm eff}$ variations, and up to 23% for [A/H] variations. These values can be considered as an estimation of errors on $\Delta W_{\rm IRT}$ due to the uncertainties in the theoretical line profiles. However, for most of the stars analyzed here, we find that the statistical noise dominates the $\Delta W_{\rm IRT}$ variations. In conclusion, we adopt the statistical errors given by Eq. (7) with the caveat that they probably represent only lower limits.

Table 4 shows the values of the *CD*, $R_{\rm IRT}$, and residual EQW measurements of the Ca II IRT lines, together with their estimated errors.

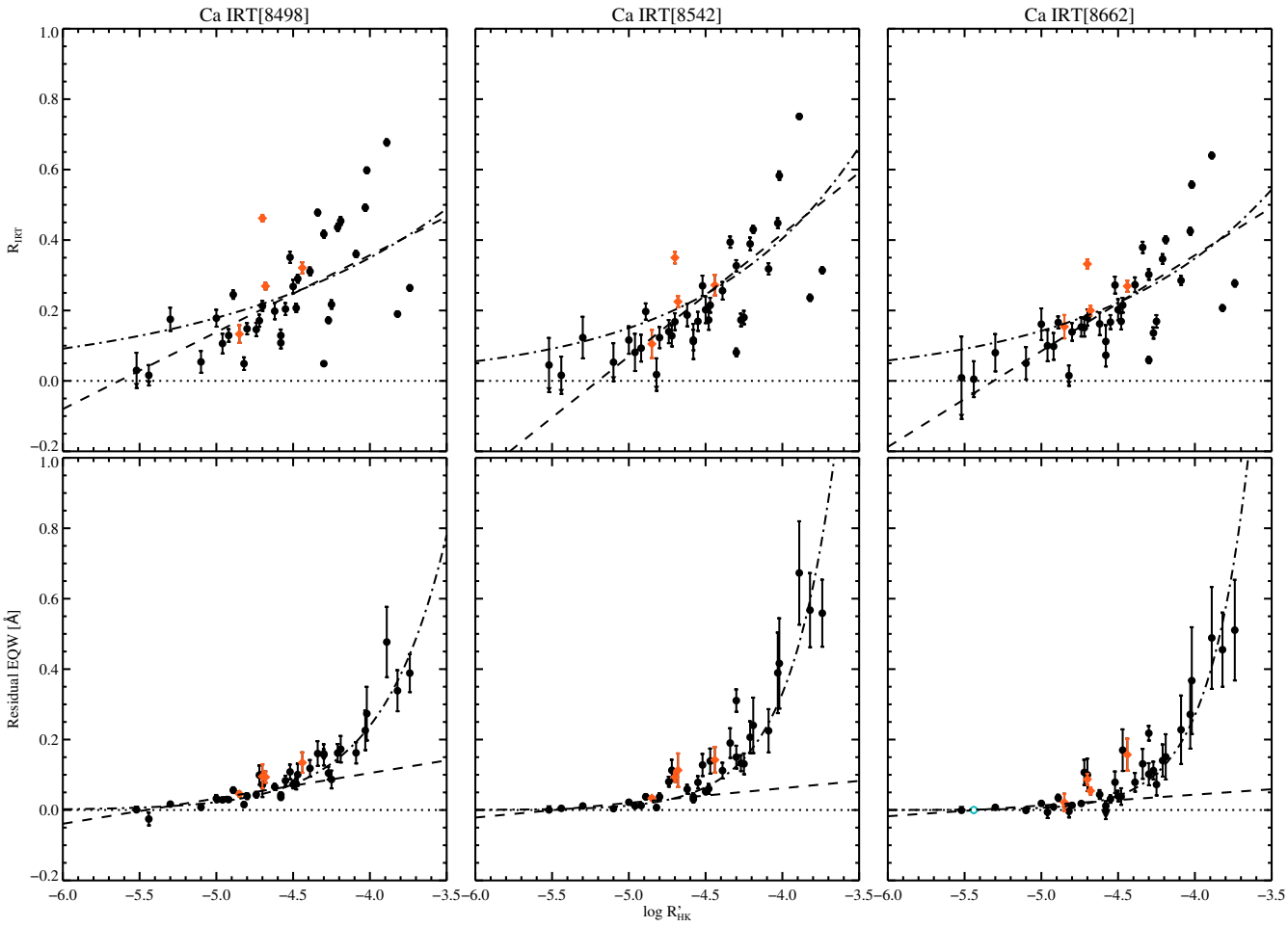

Fig. 4. The $R_{\rm IRT}$ index and the residual EQW, $\Delta W_{\rm IRT}$, versus $\log R'_{\rm HK}$ for the three components of the Ca II IRT. Grey diamonds (red in electronic version) represent data obtained for the four spectroscopic binaries (see Sect. 2). The grey open circle (blue in electronic version) in the lower right panel mark the null EQW(λ8662) measurement for HD 165807. The horizontal dotted lines highlights the separation between relatives emission and absorption.

4. Results

The residual EQW, $R_{\rm IRT}$, and $\log R'_{\rm HK}$ are all pure chromospheric diagnostics because they have been obtained after proper subtraction of the photospheric contribution. Therefore, we expect to find a close correlation of our indicators with the $\log R'_{\rm HK}$ measures. For this reason, the behavior of the $R_{\rm IRT}$ and residual EQW versus $\log R'_{\rm HK}$ was investigated for the three Ca II IRT lines.

Figure 4 shows the $R_{\rm IRT}$ index and $\Delta W_{\rm IRT}$ for the three components of the Ca II IRT, versus $\log R'_{\rm HK}$. Both relations have been fitted with a linear and with an exponential function. In the fit procedure, the four spectroscopic binaries, HD 65430, HD 68638, HD 79969, and HD 132756, have not been considered. Furthermore, we have excluded the three stars HD 26736, HD 28805, and HD 29461 from our analysis, for which, to our knowledge, there are no available $\log R'_{\rm HK}$ measurements.

The results of the linear fits for the $R_{\rm IRT}$, along with their reduced χ^2 values, χ^2_n, are the following:

$$
\begin{aligned}
R_{\rm IRT}[8498] &= 1.23 + 0.22 \times \log R'_{\rm HK} \quad \left(\chi^2_n = 206\right)\\
R_{\rm IRT}[8542] &= 1.81 + 0.35 \times \log R'_{\rm HK} \quad \left(\chi^2_n = 120\right)\\
R_{\rm IRT}[8662] &= 1.45 + 0.27 \times \log R'_{\rm HK} \quad \left(\chi^2_n = 104\right). \qquad (8)
\end{aligned}
$$

The results of the exponential fit are, on the other hand,

$$
\begin{aligned}
\log R_{\rm IRT}[8498] &= 0.71 + 0.29 \times \log R'_{\rm HK} \quad \left(\chi^2_n = 6.4\right)\\
\log R_{\rm IRT}[8542] &= 1.33 + 0.43 \times \log R'_{\rm HK} \quad \left(\chi^2_n = 3.8\right)\\
\log R_{\rm IRT}[8662] &= 1.09 + 0.39 \times \log R'_{\rm HK} \quad \left(\chi^2_n = 3.3\right). \qquad (9)
\end{aligned}
$$

The $\log$ Ca II IRT versus $\log R'_{\rm HK}$ fits above are better than the linear fits of Eqs. (8), but still not very good, as indicated by the relatively high values of χ^2_n that obviously reflect the large scatter of the data points around the mean relation, compared with the estimated errors. Some of the scattering can be explained, for instance, by considering that Ca II IRT and Ca II H & K observations are not simultaneous: the known long-term variability of chromospheric phenomena in active stars could explain the extra scatter found in the fit relations. However, in addition to this effect, it is also possible that our adopted errors are somewhat underestimated, as discussed in Sect. 3.2.

For $\Delta W_{\rm IRT}$, the linear fit yields:

$$
\begin{aligned}
\Delta W_{\rm IRT}[8498] &= 0.39 + 0.07 \times \log R'_{\rm HK} \quad \left(\chi^2_n = 6.5\right)\\
\Delta W_{\rm IRT}[8542] &= 0.23 + 0.04 \times \log R'_{\rm HK} \quad \left(\chi^2_n = 11.9\right)\\
\Delta W_{\rm IRT}[8662] &= 0.17 + 0.03 \times \log R'_{\rm HK} \quad \left(\chi^2_n = 6.9\right), \qquad (10)
\end{aligned}
$$

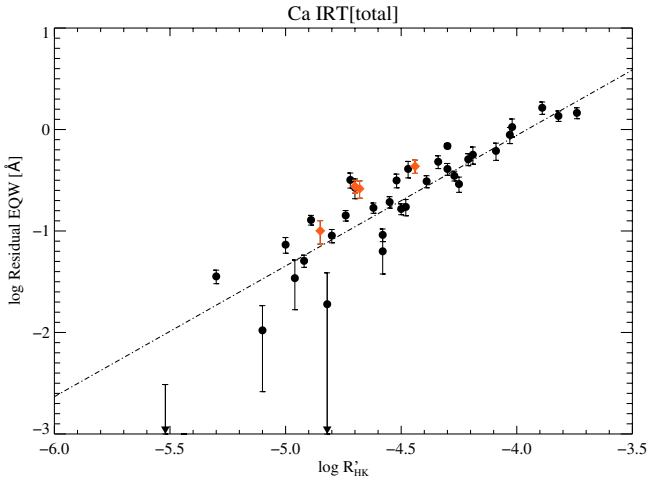

Fig. 5. The sum of residual EQWs in the three components of the Ca II IRT, $\Delta W_{\rm IRT}$[total], versus $\log R'_{\rm HK}$. As in Fig. 4, grey diamonds (red in electronic version) represent data obtained for the four spectroscopic binaries.

while, for the exponential fit, $\log \Delta W_{\rm IRT}$ versus $\log R'_{\rm HK}$, we obtain:

$$\log \Delta W_{\rm IRT}[8498] = 3.49 + 1.03 \times \log R'_{\rm HK} \quad \left(\chi^2_n = 0.085\right)$$
$$\log \Delta W_{\rm IRT}[8542] = 5.19 + 1.42 \times \log R'_{\rm HK} \quad \left(\chi^2_n = 0.15\right)$$
$$\log \Delta W_{\rm IRT}[8662] = 6.00 + 1.64 \times \log R'_{\rm HK} \quad \left(\chi^2_n = 0.11\right). \quad (11)$$

In this case, the exponential fits exhibit substantially better χ^2_n values, consistent with the visual impression given by Fig. 4 of a better representation of the correlation.

Figure 4 also hints at a tighter correlation between $\Delta W_{\rm IRT}$ and $\log R'_{\rm HK}$, compared to the correlation between $R_{\rm IRT}$ and $\log R'_{\rm HK}$. This is in fact reasonable, since we expect the errors on $\Delta W_{\rm IRT}$ to be smaller than the single-point measure represented by the $R_{\rm IRT}$ index.

We also correlate the two indexes $R_{\rm IRT}$ and $\Delta W_{\rm IRT}$ for each component of the Ca II IRT. The correlation is good, except for the three fast rotators HD 43989, HD 129674, and HD 171488. It is obvious that the residual EQW would be the same in those objects as in slower rotators with the same excess emission, while the $R_{\rm IRT}$ would be substantially reduced by rotational broadening, even if the reference theoretical, photospheric profile already takes this broadening process into account. This fact suggests that $\Delta W_{\rm IRT}$ may be a better indicator than $R_{\rm IRT}$.

Finally, it is interesting to consider the sum of the residual EQWs of the three components of the Ca II IRT, $\Delta W_{\rm IRT}$[total], since it is a quantity related to the total chromospheric radiative losses in that triplet. The correlation of $\log \Delta W_{\rm IRT}$[total] with $\log R'_{\rm HK}$ is shown in Fig. 5. The fitted relation between the two quantities is

$$\log \Delta W_{\rm IRT}[\text{total}] = 5.09 + 1.29 \times \log R'_{\rm HK} \quad (\chi^2_n = 0.23). \quad (12)$$

As was already apparent from Eqs. (11), our measurements of chromospheric excesses in the Ca II IRT correlate almost linearly with the $\log R'_{\rm HK}$ indicator, which in turn is also a proxy for the chromospheric losses in the Ca II H & K resonance doublet.

Both indexes, however, represent an excess emission relative to the local photospheric continuum. Estimation of the *absolute* excess flux, and thus the total chromospheric losses due to Ca II, would require an estimate of the stellar spectral photospheric distribution. Such an analysis is beyond the scope of this paper, but we plan to continue investigating this aspect in a future work.

5. Conclusions

Our analysis indicates that the Ca II IRT lines are good chromospheric diagnostics and both $\Delta W_{\rm IRT}$ and the $R_{\rm IRT}$ quantities can be used as chromospheric indicators. The following results are the main outcome of our analysis:

1. Given the errors in the measurements of the residual EQW and $R_{\rm IRT}$ and taking into account that the reference $\log R'_{\rm HK}$ values we adopted may reflect different activity levels of our target stars, we find that both the residual EQW ($\Delta W_{\rm IRT}$) and the $R_{\rm IRT}$ can be used as chromospheric indicators in place of the classical $\log R'_{\rm HK}$ indicator.
2. We, however, find that the $\log \Delta W_{\rm IRT}$ indicator seems more tightly correlated with $\log R'_{\rm HK}$ in our data sample. This is not entirely surprising, since (i) both indicators are related to the chromospheric radiative losses in the Ca II IRT and Ca II H & K lines, respectively, and (ii) $\Delta W_{\rm IRT}$ is the sum of more data points and thus has better *S/N* than $R_{\rm IRT}$.
3. Finally, we find that the total chromospheric excess EQW in the Ca II IRT is almost linearly correlated with the excess in the Ca II H & K doublet, as estimated through the $\log R'_{\rm HK}$ index.

Acknowledgements. I.B. wishes to thank all colleagues of the Catania Cool Stars Group (`http://www.ct.astro.it/coolstars/`). In particular, I.B. wishes to remember the beloved Prof. Marcello Rodonò who prematurely left us. The authors are also in debt to the referee, J. Linsky, for his careful reading of the manuscript and for his advice, which has led to a substantial improvement of this work. The work of R.A.C. was funded by the Italian Ministry for Scientific and Technological Research (MURST – now: MIUR), CoFin2000, while working at the Osservatorio di Capodimonte. This research has made use of the SIMBAD database, operated at CDS, Strasbourg, France.

References

Allard, F., & Hauschildt, P. H. 1995, ApJ, 445, 433
Andretta, V., Busà, I., Gomez, M. T., & Terranegra, L. 2005, A&A, 430, 669
Beers, T. C., Rossi, S., Norris, J. E., Ryan, S. G., & Shefler, T. 1999, AJ, 117, 981
Busà, I., Andretta, V., Gomez, M. T., & Terranegra, L. 2001, A&A, 373, 993
Carlsson, M. 1986, A Computer Program for Solving Multi-Level Non-LTE Radiative Transfer Problems in Moving or Static Atmospheres, Report No. 33, Uppsala Astronomical Observatory
Chen, Y. Q., Nissen, P. E., Zhao, G., Zhang, H. W., & Benoni, T. 2000, A&AS, 141, 491
Chmielewski, Y. 2000, AAp, 353, 666
Cutispoto, G., Pastori, L., Pasquini, L., et al. 2002, A&A, 384, 491
Dempsey, R. C., Bopp, B. W., Henry, G. W., & Hall, D. S. 1993, ApJS, 86, 293
Drake, J. J. 1991, MNRAS, 251, 369
Eberhard, G., & Schwarzschild, K. 1913, ApJ, 38, 292
Eggen, O. J. 1998, AJ, 115, 2397
Fekel, F. C. 1997, PASP, 109, 514
Feltzing, S., & Gustafsson, B. 1998, A&AS, 129, 237
Foing, B. H., Crivellari, L., Vladilo, G., Rebolo, R., & Beckman, J. E. 1989, A&AS, 80, 189
Gaidos, E. J., Henry, G. W., & Henry, S. M. 2000, AJ, 120, 1006
Głębocki, R., & Stawikowski, A. 2000, Acta Astronomica, 50, 509
Goldberg, D., Mazeh, T., Latham, D. W., et al. 2002, AJ, 124, 1132
Gratton, R. G., Bonanno, G., Bruno, P., et al. 2001, Experimental Astronomy, 12, 107
Gray, D. F. 1992, The observation and analysis of stellar photospheres, 2nd Ed. (Cambridge: Cambridge University Press)
Gray, R. O., Graham, P. W., & Hoyt, S. R. 2001, AJ, 121, 2159
Habing, H. J., Dominik, C., Jourdain de Muizon, M., et al. 2001, A&A, 365, 545

Hale, G. E., & Ellerman, F. 1920, PASP, 32, 272
Haywood, M. 2001, MNRAS, 325, 1365
Hempelmann, A., Schmitt, J. H. M. M., & Stępień, K. 1996, A&A, 305, 284
Henry, G. W., Fekel, F. C., & Hall, D. S. 1995, AJ, 110, 2926
Horch, E. P., Robinson, S. E., Meyer, R. D., et al. 2002, AJ, 123, 3442
Katz, D., Munari, U., Cropper, M., et al. 2004, MNRAS, 354, 1223
Kelch, W. L., Worden, S. P., & Linsky, J. L. 1979, ApJ, 229, 700
Kotoneva, E., Flynn, C., Chiappini, C., & Matteucci, F. 2002, MNRAS, 336, 879
Latham, D. W., Stefanik, R. P., Torres, G., et al. 2002, AJ, 124, 1144
Linsky, J. L. 1991, in Mechanisms of Chromospheric and Coronal Heating, ed. P. Ulmschneider, E. R. Priest, & R. Rosner, 166
Linsky, J. L., Hunten, D. M., Sowell, R., Glackin, D. L., & Kelch, W. L. 1979, ApJS, 41, 481
Messina, S., Rodonò, M., & Guinan, E. F. 2001, A&A, 366, 215
Nidever, D. L., Marcy, G. W., Butler, R. P., Fischer, D. A., & Vogt, S. S. 2002, ApJS, 141, 503
Nordström, B., Mayor, M., Andersen, J., et al. 2004, A&A, 418, 989
Osten, R. A., & Saar, S. H. 1998, MNRAS, 295, 257
Paulson, D. B., Sneden, C., & Cochran, W. D. 2003, AJ, 125, 3185
Piters, A. J. M., Schrijver, C. J., Schmitt, J. H. M. M., et al. 1997, A&A, 325, 1115
Rodonò, M. 2000, in Stellar Clusters and Associations: Convection, Rotation, and Dynamos, ed. R. Pallavicini, G. Micela, & S. Sciortino, ASP Conf. Ser., 198, 391
Santos, N. C., Israelian, G., Mayor, M., Rebolo, R., & Udry, S. 2003, A&A, 398, 363
Snider, S., Allende Prieto, C., von Hippel, T., et al. 2001, ApJ, 562, 528
Song, I., Bessell, M. S., & Zuckerman, B. 2002, A&A, 385, 862
Strassmeier, K., Washuettl, A., Granzer, T., Scheck, M., & Weber, M. 2000, A&AS, 142, 275
Taylor, B. J. 2003, A&A, 398, 731
Thorburn, J. A., Hobbs, L. M., Deliyannis, C. P., & Pinsonneault, M. H. 1993, ApJ, 415, 150
Tokovinin, A. A., & Smekhov, M. G. 2002, A&A, 382, 118
Uitenbroek, H. 1989, A&A, 213, 360
Vernazza, J. E., Avrett, E. H., & Loeser, R. 1981, ApJS, 45, 635
Wichmann, R., Schmitt, J. H. M. M., & Hubrig, S. 2003, A&A, 399, 983
Wright, C. O., Egan, M. P., Kraemer, K. E., & Price, S. D. 2003, AJ, 125, 359

Online Material

Table 4. Central depression (*CD*) measurements, $R_{\rm IRT}$ and residual equivalent width ($\Delta W_{\rm IRT}$, in mÅ) for the Ca II IRT lines.

Target	$CD_{\rm obs}[\lambda 8498]$	$R_{\rm IRT}[\lambda 8498]$	$\Delta W_{\rm IRT}[\lambda 8498]$	$CD_{\rm obs}[\lambda 8542]$	$R_{\rm IRT}[\lambda 8542]$	$\Delta W_{\rm IRT}[\lambda 8542]$	$CD_{\rm obs}[\lambda 8662]$	$R_{\rm IRT}[\lambda 8662]$	$\Delta W_{\rm IRT}[\lambda 8662]$
HD 14798	0.765 ± 0.033	0.175 ± 0.033	16.7 ± 3.2	0.853 ± 0.059	0.123 ± 0.059	11.5 ± 2.2	0.894 ± 0.053	0.080 ± 0.053	7.5 ± 3.8
HD 25998	0.464 ± 0.008	0.172 ± 0.008	104.6 ± 18.3	0.572 ± 0.018	0.173 ± 0.018	133.0 ± 22.6	0.581 ± 0.016	0.136 ± 0.016	111.9 ± 25.2
HD 26736	0.500 ± 0.012	0.351 ± 0.012	134.5 ± 27.4	0.621 ± 0.017	0.312 ± 0.017	200.0 ± 55.4	0.637 ± 0.017	0.292 ± 0.017	103.7 ± 28.1
HD 28495	0.360 ± 0.009	0.492 ± 0.009	225.9 ± 55.9	0.484 ± 0.014	0.448 ± 0.014	389.4 ± 114.4	0.504 ± 0.010	0.425 ± 0.010	271.4 ± 97.2
HD 28805	0.490 ± 0.013	0.389 ± 0.013	135.0 ± 29.1	0.602 ± 0.017	0.344 ± 0.017	232.6 ± 62.6	0.641 ± 0.016	0.300 ± 0.016	119.5 ± 33.9
HD 29461	0.584 ± 0.010	0.335 ± 0.010	94.9 ± 18.6	0.712 ± 0.025	0.256 ± 0.025	114.7 ± 24.9	0.721 ± 0.018	0.242 ± 0.018	66.7 ± 23.0
HD 31000	0.443 ± 0.009	0.360 ± 0.009	162.3 ± 30.0	0.571 ± 0.016	0.318 ± 0.016	225.0 ± 61.5	0.589 ± 0.013	0.285 ± 0.013	227.8 ± 97.2
HD 43989	0.248 ± 0.007	0.190 ± 0.007	338.7 ± 58.2	0.350 ± 0.009	0.236 ± 0.009	567.5 ± 105.4	0.343 ± 0.008	0.207 ± 0.008	455.2 ± 105.3
HD 47157	0.713 ± 0.018	0.049 ± 0.018	15.5 ± 6.3	0.832 ± 0.046	0.018 ± 0.046	7.0 ± 6.2	0.811 ± 0.029	0.015 ± 0.029	−3.5 ± 17.6
HD 58781	0.705 ± 0.016	0.148 ± 0.016	39.5 ± 8.5	0.809 ± 0.030	0.123 ± 0.030	37.4 ± 9.8	0.790 ± 0.025	0.139 ± 0.025	13.1 ± 3.7
HD 59747	0.403 ± 0.011	0.454 ± 0.011	172.7 ± 37.6	0.504 ± 0.010	0.430 ± 0.010	240.4 ± 78.7	0.530 ± 0.010	0.401 ± 0.010	151.0 ± 64.3
HD 64468	0.747 ± 0.024	0.178 ± 0.024	32.6 ± 10.2	0.854 ± 0.039	0.116 ± 0.039	22.0 ± 5.8	0.805 ± 0.045	0.161 ± 0.045	18.7 ± 5.4
HD 65430	0.727 ± 0.025	0.133 ± 0.025	45.4 ± 6.5	0.831 ± 0.040	0.105 ± 0.040	33.7 ± 6.0	0.778 ± 0.033	0.154 ± 0.033	21.3 ± 24.6
HD 68638	0.534 ± 0.009	0.269 ± 0.009	93.4 ± 15.9	0.664 ± 0.016	0.225 ± 0.016	113.1 ± 47.4	0.674 ± 0.014	0.200 ± 0.014	54.4 ± 10.0
HD 72760	0.432 ± 0.010	0.436 ± 0.010	161.9 ± 25.6	0.551 ± 0.018	0.389 ± 0.018	206.6 ± 45.2	0.590 ± 0.014	0.346 ± 0.014	140.5 ± 45.5
HD 72946	0.674 ± 0.012	0.245 ± 0.012	56.3 ± 8.3	0.771 ± 0.023	0.197 ± 0.023	37.6 ± 7.0	0.784 ± 0.017	0.166 ± 0.017	34.5 ± 8.9
HD 76752	0.709 ± 0.019	0.146 ± 0.019	43.6 ± 7.8	0.794 ± 0.033	0.140 ± 0.033	80.3 ± 14.1	0.777 ± 0.027	0.153 ± 0.027	18.4 ± 5.2
HD 76780	0.689 ± 0.016	0.108 ± 0.016	42.7 ± 6.7	0.769 ± 0.029	0.116 ± 0.029	37.1 ± 10.3	0.796 ± 0.032	0.073 ± 0.032	11.8 ± 4.3
HD 79969	0.548 ± 0.016	0.321 ± 0.016	134.6 ± 28.9	0.667 ± 0.029	0.272 ± 0.029	142.4 ± 36.3	0.668 ± 0.016	0.269 ± 0.016	157.1 ± 45.3
HD 81040	0.594 ± 0.011	0.290 ± 0.011	100.5 ± 31.1	0.734 ± 0.021	0.215 ± 0.021	138.8 ± 35.6	0.728 ± 0.021	0.215 ± 0.021	169.9 ± 59.1
HD 82443	0.219 ± 0.008	0.598 ± 0.008	273.6 ± 76.1	0.316 ± 0.012	0.583 ± 0.012	416.3 ± 128.1	0.328 ± 0.009	0.557 ± 0.009	367.3 ± 151.7
HIP 46854	0.851 ± 0.050	0.030 ± 0.050	0.7 ± 2.4	0.900 ± 0.077	0.045 ± 0.077	0.3 ± 0.9	0.918 ± 0.117	0.009 ± 0.117	−0.9 ± 1.5
HD 91148	0.639 ± 0.012	0.207 ± 0.012	74.2 ± 15.7	0.757 ± 0.028	0.173 ± 0.028	60.2 ± 13.7	0.757 ± 0.023	0.169 ± 0.023	38.3 ± 23.6
HD 94765	0.447 ± 0.008	0.478 ± 0.008	160.4 ± 35.1	0.576 ± 0.016	0.394 ± 0.016	190.2 ± 42.1	0.587 ± 0.016	0.379 ± 0.016	131.0 ± 42.5
HD 96937	0.723 ± 0.017	0.129 ± 0.017	36.1 ± 7.4	0.820 ± 0.050	0.112 ± 0.050	30.4 ± 9.2	0.816 ± 0.046	0.112 ± 0.046	−3.4 ± 22.5
HD 98736	0.767 ± 0.028	0.106 ± 0.028	28.8 ± 4.4	0.861 ± 0.053	0.081 ± 0.053	11.6 ± 2.4	0.839 ± 0.044	0.100 ± 0.044	−6.1 ± 16.8
HD 105631	0.652 ± 0.019	0.268 ± 0.019	72.9 ± 11.4	0.766 ± 0.038	0.202 ± 0.038	52.3 ± 7.6	0.762 ± 0.030	0.202 ± 0.030	39.7 ± 14.9
HD 108574	0.580 ± 0.012	0.217 ± 0.012	86.7 ± 25.2	0.706 ± 0.019	0.180 ± 0.019	131.0 ± 29.6	0.701 ± 0.018	0.169 ± 0.018	72.4 ± 31.1
HD 110833	0.574 ± 0.016	0.351 ± 0.016	108.3 ± 20.7	0.700 ± 0.029	0.270 ± 0.029	127.9 ± 31.5	0.694 ± 0.024	0.272 ± 0.024	78.8 ± 30.6
HD 112742	0.816 ± 0.031	0.054 ± 0.031	7.8 ± 7.0	0.887 ± 0.054	0.053 ± 0.054	3.9 ± 1.9	0.887 ± 0.046	0.050 ± 0.046	−1.2 ± 3.1
HD 116442	0.691 ± 0.017	0.171 ± 0.017	99.1 ± 27.2	0.809 ± 0.030	0.128 ± 0.030	112.7 ± 29.9	0.779 ± 0.025	0.151 ± 0.025	106.8 ± 35.8
HD 119332	0.649 ± 0.017	0.204 ± 0.017	83.3 ± 14.2	0.763 ± 0.027	0.169 ± 0.027	78.5 ± 17.5	0.762 ± 0.020	0.167 ± 0.020	31.1 ± 10.6
HD 122676	0.642 ± 0.014	0.213 ± 0.014	71.8 ± 35.0	0.766 ± 0.024	0.168 ± 0.024	95.6 ± 11.9	0.750 ± 0.023	0.180 ± 0.023	99.7 ± 46.0
HD 128311	0.433 ± 0.010	0.417 ± 0.010	156.6 ± 30.0	0.602 ± 0.016	0.327 ± 0.016	150.2 ± 32.3	0.624 ± 0.015	0.302 ± 0.015	101.7 ± 31.4
HD 129674	0.195 ± 0.006	0.049 ± 0.006	159.5 ± 13.0	0.368 ± 0.011	0.081 ± 0.011	310.7 ± 31.6	0.332 ± 0.009	0.059 ± 0.009	218.0 ± 20.8
HD 131023	0.545 ± 0.011	0.311 ± 0.011	118.2 ± 23.7	0.678 ± 0.025	0.256 ± 0.025	111.8 ± 22.4	0.658 ± 0.021	0.273 ± 0.021	78.7 ± 26.4
HD 132756	0.457 ± 0.009	0.462 ± 0.009	95.2 ± 34.3	0.618 ± 0.016	0.350 ± 0.016	93.5 ± 13.3	0.631 ± 0.013	0.332 ± 0.013	87.1 ± 15.5
HD 149806	0.654 ± 0.023	0.198 ± 0.023	66.0 ± 8.4	0.744 ± 0.032	0.187 ± 0.032	59.1 ± 12.4	0.766 ± 0.032	0.162 ± 0.032	44.0 ± 12.6
HD 164922	0.732 ± 0.018	0.129 ± 0.018	29.4 ± 4.2	0.844 ± 0.038	0.093 ± 0.038	12.6 ± 3.8	0.835 ± 0.038	0.098 ± 0.038	8.8 ± 4.1
HD 165807	0.809 ± 0.029	0.016 ± 0.029	−25.6 ± 18.1	0.886 ± 0.053	0.016 ± 0.053	4.7 ± 2.5	0.884 ± 0.051	0.005 ± 0.051	0.0 ± 0.0
HD 171488	0.218 ± 0.008	0.264 ± 0.008	388.6 ± 53.9	0.306 ± 0.009	0.314 ± 0.009	558.8 ± 95.2	0.309 ± 0.009	0.277 ± 0.009	510.7 ± 142.8
HD 175742	−0.001 ± 0.009	0.677 ± 0.009	477.0 ± 99.9	0.028 ± 0.007	0.751 ± 0.007	673.1 ± 146.8	0.113 ± 0.008	0.640 ± 0.008	488.6 ± 144.7